Chinese Chemical Letters 36 (2025) 109772

Contents lists available at ScienceDirect

Chinese Chemical Letters

journal homepage: www.elsevier.com/locate/cclet

Self-assembled ultrathick MoS_2 conductive hydrogel membrane *via* ionic gelation for superior capacitive energy storage

Yayun Shi[a], Congcong Liu[b,*], Zhijun Zuo[a,*], Xiaowei Yang[c,*]

[a] State Key Laboratory of Clean and Efficient Coal Utilization, Taiyuan University of Technology, Taiyuan 030024, China
[b] Flexible Electronics Innovation Institute, Jiangxi Science and Technology Normal University, Nanchang 330013, China
[c] School of Chemistry and Chemical Engineering, Shanghai Jiao Tong University, Shanghai 200240, China

ARTICLE INFO

Article history:
Received 16 January 2024
Revised 3 March 2024
Accepted 14 March 2024
Available online 16 March 2024

Keywords:
Capacitive electrodes
Channel structure
2D inorganic nanosheets
Ionic transport
MoS_2 hydrogel membranes

ABSTRACT

Conductive hydrogel membranes with nanofluids channels represent one of the most promising capacitive electrodes due to their rapid kinetics of ion transport. The construction of these unique structures always requires new self-assembly behaviors with different building blocks, intriguing phenomena of colloidal chemistry. In this work, by delicately balancing the electrostatic repulsions between 2D inorganic nanosheets and the electrostatic adsorption with cations, we develop a general strategy to fabricate stable free-standing 1T molybdenum disulphide (MoS_2) hydrogel membranes with abundant fluidic channels. Given the interpenetrating ionic transport network, the MoS_2 hydrogel membranes exhibit a high-level capacitive performance 1.34 F/cm^2 at an ultrahigh mass loading of 11.2 mg/cm^2. Furthermore, the interlayer spacing of MoS_2 in the hydrogel membranes can be controlled with ångström-scale precision using different cations, which can promote further fundamental studies and potential applications of the transition-metal dichalcogenides hydrogel membranes.

© 2025 Published by Elsevier B.V. on behalf of Chinese Chemical Society and Institute of Materia Medica, Chinese Academy of Medical Sciences.

As an important class of electrode materials, two-dimensional materials, such as transition metal dichalcogenides (2D TMDs), graphene-based materials, and transition metal carbide (MXene) have attracted large attentions in energy storage and conversion [1]. Among them, molybdenum disulphide (MoS_2) have great potentials for electrochemical energy storage applications thanks to their high stacking density, chemical stability, economical efficient, and adjustable electrical conductivity [1–4]. Despite the 2D graphene-like structure, the MoS_2 nanosheets are much more rigid out of plane due to the three-atomic-layered structure, together with their strong inter-sheet van der Waals force, thereby leading to the irreversible restacking [5], which results in insufficient ion diffusion especially in thick electrodes with high mass loading (*e.g.*, 10 mg/cm^2) that approaches the practical level [6,7]. The ionic conductivity has been improved by *in-situ* growing vertically aligned MoS_2 or developing heterostructures [8–10], but it is limited by high preparation costs and expensive materials. Whereas self-assembly by exploiting interaction between nanosheets is a cost-effective, convenient, and scale-up-friendly method. Hence, a more practical strategy is to modify the inter-nanosheets interaction to improve the stacking structure of membranes for facilitating ionic conduction and energy storage properties.

During the self-assembly process of solution-processable 2D nanosheets, the water can serve as a particularly effective "spacer" to tackle the fatal issue of the restacking in the application of supercapacitors [11,12]. The highly porous structure with pervading fluid channels provides abundant pathways for the electrolyte-ion transporting onto the surface of individual nanosheets [13–15]. It has been reported that the hydrogelation of graphene-based 2D laminated membranes enhanced ionic diffusion coefficient by ~9.4 times [12], and the outstanding capacitive performances are also achieved even with the high mass loading [16,17]. For example, the 2D materials-based hydrogel membrane (MGH) with an area loading of 2.97 mg/cm^2 shows a capacity retention of 89.5% (319.6 F/g) at 100 mV/s, illustrating its excellent rate capability and specific capacitance [18]. In a case study of oriented-graphene hydrogel membranes, the unique π-conjugated structure and corrugated configuration of chemically converted graphene are the crucial properties for constructing the unusual structures that can trap a significant amount of water in the membrane [16,19,20]. It has been previously shown that a stable MoS_2 colloidal suspension without any surfactants can form through exfoliation of Li-intercalated MoS_2 [21,22], owing to the strong electrostatic repulsion of negative charge that originates from the electron injection

* Corresponding authors.
E-mail addresses: lcc.0705@jxstnu.edu.cn (C. Liu), zuozhijun@tyut.edu.cn (Z. Zuo), yangxw@sjtu.edu.cn (X. Yang).

https://doi.org/10.1016/j.cclet.2024.109772
1001-8417/© 2025 Published by Elsevier B.V. on behalf of Chinese Chemical Society and Institute of Materia Medica, Chinese Academy of Medical Sciences.

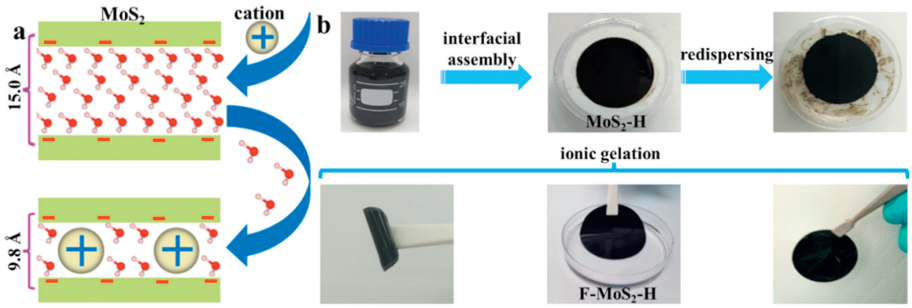

Fig. 1. The assembly strategy of the F-MoS_2-H membrane. (a) Schematic diagram of the cation mediated gelation mechanism. (b) Photograph showing the ionic gelation process of F-MoS_2-H membrane from MoS_2 dispersion.

during lithium intercalation [23–26]. It provided the basis for the development of MoS_2 hydrogel membranes, but the development of hydrogel membranes is still lacking. Until now, little is known about the experimental investigation of MoS_2 membranes with confined fluids because of the difficulties in constructing hydrogel membrane by adopting the similar manners to the graphene, as the result of the absence of π-conjugated structure and corrugated configuration for MoS_2 nanosheets. Consequently, a uniquely assembly strategies will be needed to create TMDs hydrogel materials for the purposes of understanding their assembly behaviors and further electrochemical energy storage.

The crucial point in the assembly of TMDs hydrogel membranes is to modulate the strong interactions between the nanosheets and to avoid uncontrolled redispersion in aqueous solution. In addition to the interaction between nanosheets and water molecules, the charged cations have good affinity with MoS_2 nanosheets, which can be employed to mediate the structure of MoS_2 membranes. In the present work, taking the negatively charged metallic-phase MoS_2 nanosheets as the building blocks, we employed cations as the gelators in free-standing and highly-conductive MoS_2 hydrogel membranes with nanoconfined water by delicately balancing the electrostatic repulsion between the 2D nanosheets (Fig. 1a), and studied their electrochemical properties. With the interpenetrating ion diffusion paths, this conductive MoS_2 hydrogel membrane electrode demonstrates greatly improved ion-transport properties, leading to high-level capacitive performance at high mass loadings (up to 11.2 mg/cm^2). This strategy provides a novel route of constructing TMD hydrogel membranes, and promotes the further application of TMDs materials in the field of electrochemical energy storage.

Fabrication of the free-standing MoS_2 hydrogel (F-MoS_2-H) membrane: MoS_2 colloidal solution was prepared by lithium intercalation into MoS_2 powder and chemically exfoliated as reported previously [3]. The X-ray photoelectron spectroscopy (XPS) spectrums of elemental S and Mo in MoS_2 before and after chemically exfoliation were compared to demonstrate the phase of MoS_2 (Fig. S1 in Supporting information). Compared to the XPS spectrums of bulk MoS_2 (S $2p_{1/2}$: 163.6 eV, S $2p_{3/2}$: 162.5 eV, $Mo3d_{3/2}$: 232.5 eV, Mo $3d_{5/2}$: 229.6 eV), there are new peaks appeared at low binding energy region (S $2p_{1/2}$: 162.0 eV, S $2p_{3/2}$: 160.8 eV, $Mo3d_{3/2}$: 231.1 eV, Mo $3d_{5/2}$: 228.0 eV) in the XPS spectrums of exfoliated MoS_2, which is consistent with the 1T phase MoS_2 in previous researches [23]. And it proves that MoS_2 nanosheets contained 72% 1T phase have been successfully prepared. As-obtained MoS_2 dispersion was vacuum filtrated through the mixed cellulose ester filter membrane (0.05 μm pore size). The vacuum was disconnected immediately once no MoS_2 dispersion was left on the filtrate membrane, and the MoS_2 hydrogel (MoS_2-H) is produced. After that, the filter membrane with MoS_2-H was immersed into the 5 vol% BMIM-BF_4 aqueous solution, where the ions would intercalation the interlayer between MoS_2 nanosheets gradually and form the free-standing F-MoS_2-H. Finally, the F-MoS_2-H can be carefully peeled off from the filter membrane. The same method was also applied to prepare F-MoS_2-H membranes in saline solution (1.0 mol/L) with different cations. And for comparation, a completely dried MoS_2 (D-MoS_2) membrane was constructed by vacuum filtrated and drying.

Zeta potential studies of MoS_2 nanosheets was determined using a Nano-ZS 90 Nanosizer (Malvern Instruments Ltd., Worcestershire, UK). Scanning electron microscope (SEM) imaging of the cross section for MoS_2 membranes were performed using a field emission SEM system (JSM 6701F). High resolution transmission electron microscope (HRTEM) characterization was performed using an aberration-corrected JEOL JEM-ARM 200CF STEM equipped with a 200 keV cold-field emission gun. The Raman spectra was obtained *via* a RENISHAW inVia Raman microscope (Wotton-under-Edge, UK). The X-ray diffraction (XRD) patterns were recorded at ambient temperature on a Bruker D8 Advance diffractometer at 40 kV, 40 mA for Cu Kα ($\lambda = 1.5418$ Å), with a scan speed of 1 s/step, a step size of 0.02° in 2θ. The GIWAXS characterization was performed by a simultaneous WAXS acquisition using a Xeuss 2.0 WAXS system (Xenocs, Sassenage, France) with a PILATUS3 R 1M detector. The details for DFT calculation are provided in Supporting information.

The electrochemical experiments were carried out in plastic Swagelok cells with 1.0 mol/L H_2SO_4 electrolyte by a Bio-Logic VMP3 multi-channel potentiostat/galvanostat. Two Pt plate electrodes and filter paper were used as current collectors and separator. The F-MoS_2-H membranes were directly used as electrodes without adding any other polymeric binders or conductive additives. Note that all the electrodes were exchanged with the electrolyte solution for 3 h prior to test. Before electrochemical performance was recorded, cyclic voltammetry (CV) scanning with a rate of 50 mV/s was conducted for several cycles to stabilize the electrodes. The details for calculation of capacitance are provided in Supporting information.

As shown in Fig. 1b, the MoS_2-H membrane attached to a filter membrane was prepared by solid/liquid interfacial assembly of the solution-processable MoS_2 nanosheets. After drying, face-to-face restacking inevitably occurs in the membrane due to the van der Waals attraction. However, it is noted that the MoS_2-H membrane is unstable and quickly re-dispersed in deionized water because of the hydration forces and electrostatic repulsions, similar to that of the graphene oxide [27]. By contrast, the stable F-MoS_2-H membrane with about 85 wt% liquid is formed when the H-MoS_2 membrane was soaked in ionic liquids (ILs, 1–butyl–3-methylimidazolium tetrafluoroborate, BMIM-BF_4) aqueous solution. And it is demonstrated that F-MoS_2-H can retain the structural integrity in both acidic and alkali solutions, and withstand vigorous mechanical agitation in water (Fig. 1b and Fig. S3 in Supporting information), the stability of which is improved significantly compared to that of the MoS_2-H membrane.

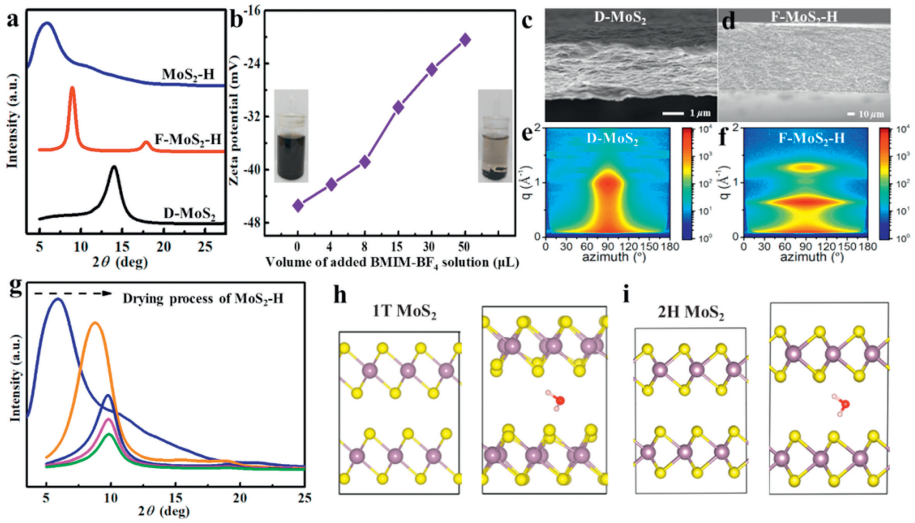

Fig. 2. The structural analysis of F-MoS_2-H membrane. (a) XRD patterns of as-prepared MoS_2-H, F-MoS_2-H and D-MoS_2 membranes. (b) Zeta potential of MoS_2 nanosheets *vs.* volume of added BMIM-BF_4 (volume ratio of 5%) in 15 mL MoS_2 aqueous dispersions with a concentration of 0.02 mg/mL. (c, d) SEM images of cross sections of D-MoS_2 and F-MoS_2-H membranes. (e, f) 2D raw scattering pattern of the GIWAXS of the D-MoS_2 and F-MoS_2-H membranes. To maintain the liquid environment, the F-MoS_2-H membranes were completely exchanged with pure BMIM-BF_4 before the SEM and GIWAXS test. (g) XRD patterns of MoS_2-H membrane in the drying process at room temperature. The configuration diagrams of (h) 1T MoS_2 and (i) 2H MoS_2 interlayer with and without H_2O in DFT calculations.

For the further analysis of the assembly mechanism of 2D MoS_2 nanosheets with ILs, the X-ray diffraction (XRD) is performed to character the nanostructure of membrane. A broad (002) peak of the H-MoS_2 membrane reveals an interlayer spacing of ~15 Å (Fig. 2a), 8.7 Å larger than that of bulk MoS_2, signifying the presence of plentiful interlayered water between individual MoS_2 nanosheets [5]. The introduction of BMIM-BF_4 leads the (002) peak obviously shifts to 9° in H-MoS_2 membrane, suggesting a 35% decrease in the interlayer distance from 15.0 Å of H-MoS_2 to 9.8 Å of the F-MoS_2-H membrane (Fig. 2b). The above assembly behavior can be explained by analyzing the colloidal forces between MoS_2 nanosheets and the ionic gelation mechanism. Based on the extended Derjaguin–Landau–Verwey–Overbeek (DLVO) theory, the equilibrium interlayer spacing of H-MoS_2 membrane is controlled by the van der Waals attraction, electrostatic repulsion and hydration force [28]. When MoS_2-H membrane soaked into the water again, the repulsive electrostatic interaction force would be dominant because of the large anionic polarizability that arises from the S^{2-} [29], leading to the redispersion (Fig. 1b). In contrast, as $BMIM^+$ inserted into the interlayers of MoS_2-H membrane, the adsorption force ($E_{ad} = -6.6$ eV) between the cations and MoS_2 nanosheets partially shield the electrostatic repulsion between nanosheets, preventing the redispersion. Meanwhile, the cross-linking effect of ions between nanosheets strengthens the anti-swelling ability and mechanical properties of membranes. The synergistic effect of both shielding effect and cross-linking effect promotes the gelation of F-MoS_2-H membrane. In order to further prove the charge screening mechanism, we investigate the variation of surface charge (zeta potential) of MoS_2 nanosheets with increasing concentrations of ILs (Fig. 2b). Obviously, the zeta potential increases gradually with the increase of ILs. An immediate coagulation behavior can be observed as the zeta potential increases above −20 mV, which is consistent with the colloid theory. This ionic gelation improves the mechanical performance and stability of the membrane, so that it remains integrity and stable whether immersed in acid or alkaline solutions for 7 days (Fig. S3).

Compared to the completely D-MoS_2 membrane, the F-MoS_2-H membrane have more favorable and connective structure. Specifically, owing to the intercalation of cations and water in the negatively-charged MoS_2 nanosheets, the high-resolution transmission electron microscope (HRTEM) images of F-MoS_2-H membrane prove the expansion of interlayer distance relative to that of completely D-MoS_2 membrane (Fig. S4 in Supporting information). Studies with side view of D-MoS_2 membrane under scanning electron microscopy (SEM) show a layered and tightly-packed structure as a result of the van der Waals attractions between MoS_2 nanosheets (Fig. 2c). Obviously, there is a porous layered packed structure for F-MoS_2-H membrane (Fig. 2d and Fig. S5 in Supporting information). It is consistent to that the D-MoS_2 membrane has a pearly luster, while the F-MoS_2-H membrane is opaque black. The metallic luster is indicative of more uniform stacking and relatively smooth surface which is able to directly reflect the light, while the opaque surface of F-MoS_2-H indicates larger interlayer spacing/pores that would cause more diffuse reflection. The grazing incidence wide-angle X-ray scattering (GIWAXS) 2D patterns of the membranes (through-the-edge) are used to reveal classic face-on stacking of nanosheets [30,31]. Relative to the preferred parallel-oriented lamellar structures in the plane of D-MoS_2, the F-MoS_2-H membrane displays less ordered 2D raw scattering signal, indicating the arrangement of MoS_2 nanosheets tends to be porous (Figs. 2e and f, Fig. S6 in Supporting information). The favorable structure of F-MoS_2-H is attributed to the suitable amount of interlayered water.

To further investigate the distribution and state of water in the F-MoS_2-H membrane, we performed XRD patterns to observe the structural changes during drying process (Fig. 2g). It can be seen that the completely hydrogel membrane MoS_2-H contains a large interlayer spacing and plenty of water, which is expelled from the interlayers as time goes on and leads to the decreasing of interlayer spacing. After thoroughly dried, the interlayer distance reaches 8.8 Å, 2.5 Å larger than the completely dried D-MoS_2 membranes without $BMIM^+$ or water intercalation, indicating a few of interlayered water are still preserved. It is also evidenced by density functional theory (DFT) calculations. Fig. 2h show the -H of water molecule prefer to adsorb on top of the S atoms, leading to the expanding of the interlayer spacing by 1.2 Å. The water molecules are adsorbed on the 1T MoS_2 interlayer with an adsorption energy of 2.2 eV (Fig. 2i and Table S1 in Supporting information). In comparison, the water adsorption energy on the 2H phase MoS_2 interlayer (1.09 eV) is lower. And the XPS spectrum shows

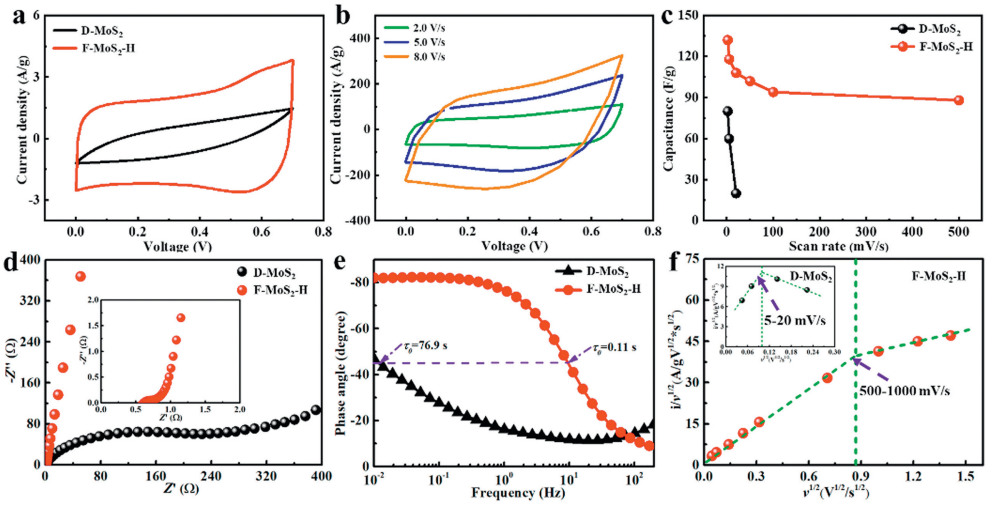

Fig. 3. Electrochemical characterization of D-MoS_2 and F-MoS_2-H membranes. (a) CV curves of D-MoS_2 and F-MoS_2-H at 50 mV/s. (b) CV curves of F-MoS_2-H membranes at 2.0–8.0 V/s. (c) Specific capacitance of D-MoS_2 and F-MoS_2-H with different scan rates. (d) Nyquist plots and (e) Bode plots of D-MoS_2 and F-MoS_2-H. (f) The correlation of $i/v^{1/2}$ *versus* $v^{1/2}$ calculated from CV curves.

that content of 2H phase MoS_2 in membrane is only ~28%. Both of these properties indicate that the channels constructed by 1T MoS_2 are the mainly modified region for ion transport and storage. It is consistent with the experimental results (Fig. 2a), where the bulk water is removed from the interlayers of MoS_2 and the confined two layers of adsorbed water are still preserved in the interlayer spacing of 9.8 Å (Fig. 1a).

To feature the ion transport behaviors, electrochemical performances of the F-MoS_2-H and dried MoS_2 membranes were carried out by symmetric supercapacitors in 1.0 mol/L H_2SO_4 electrolyte. The Raman peaks of J_1, J_2, and J_3 are retained in the hydrogel membrane (Fig. S8 in Supporting information), which are only active in 1T phase MoS_2 [32], indicating a good electrical conductivity maintained and the suitability in electrochemical application. The cycle voltammetry (CV) curve of the supercapacitor with dried MoS_2 electrode delivers poor capacitive behavior (Fig. 3a). Meanwhile, the specific capacitances of D-MoS_2 electrode drastically decrease from 80 F/g to 20 F/g with the current density increases from 2 mV/s to 20 mV/s. By contrast, the F-MoS_2-H electrode reveals gratifying capacitive properties, a capacitance of 135 F/g was obtained at scan rate of 2 mV/s; particularly the difference performance becomes very pronounced at higher operation rates (Fig. 3c). The CVs profile of F-MoS_2-H electrode still remains a near-rectangular shape at an ultrafast scan rate of 8.0 V/s (Fig. 3b). The unique role of the hydrogel structure of F-MoS_2-H can also be proved by the electrochemical impedance spectroscopy (EIS) at open circuit potential over the frequency range from 100 kHz to 10 mHz. As shown in Fig. 3d, the D-MoS_2 electrode shows a large semicircle and distinct −45° line in the low frequency region [33], revealing a very slow ion diffusion and poor capacitance. In contrast, the Nyquist plot of F-MoS_2-H electrode exhibits shorter Warburg region and smaller semicircle, indicating the fastest ion transport. The improvement is also illustrated from the Bode plots that the time constant ($\tau_0 = 1/f_0$) at phase angle of 45° decreases from 76.9 s to 0.11 s, giving a shift of τ_0 by a factor near 700 (Fig. 3e). Due to the porous structural property of F-MoS_2-H electrode [1,2], we studied the CV curves in a wide range of scan rates by plotting the relationship between $i/v^{1/2}$ and $v^{1/2}$ to analyze the kinetics of the ion transport in the electrode materials, where i is the discharge current at 0.35 V and v is the scan rate [34,35]. As shown in Fig. 3f, at low scan rates from 2 mV/ s to 500 mV/s, the $i/v^{1/2}$ and $v^{1/2}$ plots are still linear with an intercept near zero. This result illustrates that it still behaves in a good capacitive manner even at high scan rates due to the highly connectivity porous structure of F-MoS_2-H membrane with appropriately expanded interlayer spacing, allowing the electrolyte ions to easily access to the surface of individual nanosheets. By contrast, the D-MoS_2 electrode clearly reveals a critical transition region at very low scan rates of 5–20 mV/s. This response is attributed to the limited channel structure, which impedes the ion transport by hindering its diffusion pathways, significantly slowing down the charge storage process. The supercapacitors based on the F-MoS_2-H electrode displays good cycle stability retaining nearly 93% of the initial capacitance after 5000 cycles at the scan rate of 500 mV/s (Fig. S10 in Supporting information).

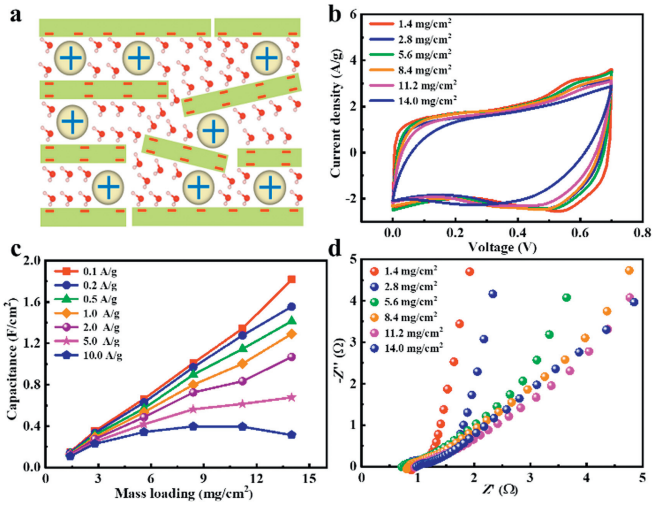

Fig. 4. The Electrochemical capability of F-MoS_2-H membrane with high mass loading. (a) Schematic diagram of F-MoS_2-H membrane in nanoscale. (b) CV curves of F-MoS_2-H electrode with different mass loadings at 50 mV/s. (c) The correlation of areal capacitance with different mass loading at various current density for the F-MoS_2-H electrode. (d) Nyquist plots of F-MoS_2-H membranes with different mass loadings.

The advantages of excellent electron transfer and rapid ion transport for F-MoS_2-H membrane is proposed to deliver high-areal capacitive performance under high mass loadings, which signifies a critical step toward to the practical applications (Fig. 4a). The CV curves of the F-MoS_2-H electrode show a relatively small

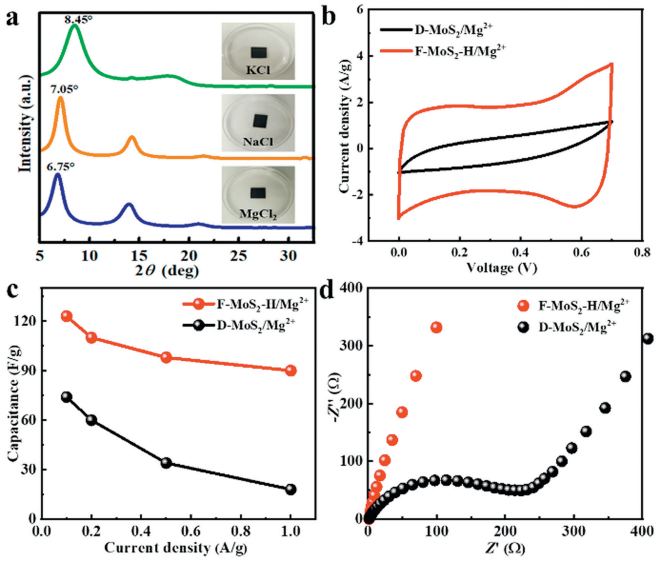

Fig. 5. The universality of the ionic gelation strategy. (a) XRD patterns of F-MoS_2-H membrane gelatinized by various cations (K^+, Na^+, and Mg^{2+}). (b) CV curves of F-MoS_2-H/Mg^{2+} and D-MoS_2-H/Mg^{2+} membranes at 50 mV/s. (c) Specific capacitance with different current density. (d) Nyquist plots of F-MoS_2-H/Mg^{2+} and D-MoS_2-H/Mg^{2+} membranes.

capacity loss at various rates induced by the increase of mass loadings (Fig. 4b), suggesting a much lower internal resistance of the porous hydrogel structure. Fig. 4c shows the relationship between areal capacitance and mass loading at a large range of current densities. The areal capacitance increases linearly with the increase of mass loadings when the current density is below 56 mA/cm^2 (5 A/g). The F-MoS_2-H electrode with 11.2 mg/cm^2 loading leads to a specific capacitance of 1.34 F/cm^2 at a current density of 1.12 mA/cm^2 (0.1 A/g). As the current density increases to 56 mA/cm^2, a value of 0.61 F/cm^2 is still maintained for the same hydrogel architecture. Although the highest mass loading (14 mg/cm^2 here) presents a larger areal capacitance of 1.8 F/cm^2 at low current density of 1.12 mA/cm^2, for the electrode (11.2 mg/cm^2), the deviations from linearity emerges as the areal capacitance reach a plateau at 56 mA/cm^2 and produce a slight decrease in the areal capacitance at 112 mA/cm^2 (10 A/g). The limiting condition of plateau-like response can be interpreted that the penetration depth of ionic current is being reached and the higher mass loading becomes progressively less beneficial [8]. As shown in the Nyquist plot (Fig. 4d), the intrinsic resistance and the Warburg region increase slightly even at a high mass loading. In the field of MoS_2-based electrode for supercapacitors (Table S2 in Supporting information), the achievement of high-level areal capacity (1340 F/cm^2 at 1.12 mA/cm^2) with high mass loadings (11.2 mg/cm^2) is outstanding, which should be ascribed to the sufficient transport pathway for both the electron transfer and ion diffusion in this hydrogel structure.

To verify the universality of the strategy, we have also prepared F-MoS_2-H membranes by alkali-metal ions with different ion radius. The XRD patterns of the stable hydrogel membranes show that the insertion process with these cation produces a systematic control of interlayer spacing from 10.5 Å in the F-MoS_2-H/K^+ to 12.5 Å in the F-MoS_2-H/Na^+ and 13.1 Å in the F-MoS_2-H/Mg^{2+} membranes, suggesting that these cations can knock out different amounts of interlayered water by ionic gelation effect (Fig. 5a). Supercapacitors based on the conductive F-MoS_2-H directly as the electrode also exhibit good capacitive performance (Fig. S11 in Supporting information). The indispensable role of confined water is further proved by analyzing the electrochemical performances of F-MoS_2-H/Mg^{2+} membranes before and after drying. Obviously, the interlayer spacing of F-MoS_2-H/Mg^{2+} hydrogel membrane decreased to 11.4 Å in the dried MoS_2/Mg^{2+} (D-MoS_2/Mg^{2+}) membrane with the removal of confined water (Fig. S12 in Supporting information). The CV curves and specific capacitance manifest better performances for the F-MoS_2-H/Mg^{2+} hydrogel compared with the dried counterpart (Figs. 5b and c). The similar result is confirmed by the Nyquist plots (Fig. 5d). It is worth pointing out that the interlayer spacing of D-MoS_2/Mg^{2+} membrane is larger than that of the $BMIM^+$ ion-based F-MoS_2-H membrane, but the capacitive performance is significantly lower. The above results suggest that the expanded interlayer spacing only caused by intercalation of cation may not be the primary factor of capacitance utilization in 2D TMDs membranes, combing with the introduction of an amount of confined water to form a highly porous hydrogel structure is the key to ensure the fast kinetics of electrolyte-ion transport.

In summary, we have developed a general strategy to fabricate F-MoS_2-H membrane by ionic gelation. Our results clearly highlight the charge screening or ionic gelation mechanism to balance the colloidal forces with cations in assembling the hydrated MoS_2 nanosheets, and explore the distribution of water molecule in the membranes. Supercapacitors based on the free-standing hydrogel membranes demonstrate a record areal-capacitance of 1.34 F/cm^2 for the MoS_2-based electrode materials at the high mass loading of 11.2 mg/cm^2, as well as the good rate capacity. Furthermore, the interlayer spacing of MoS_2 hydrogel membranes can be controlled with ångström-scale precision using different cations. This unique 2D TMDs hydrogel promises a large range of other fundamental studies of structure control and applications, such as sensors, actuators, nanofluidics, water purification and energy harvesting devices.

Declaration of competing interest

There are no conflicts of interest to declare.

Acknowledgments

This work was supported by the National Natural Science Foundation of China (Nos. 22078214, 21905206, and 22065013), and Special Fund for Science and Technology Innovation Team of Shanxi Province (No. 202204051001009).

Supplementary materials

Supplementary material associated with this article can be found, in the online version, at doi:10.1016/j.cclet.2024.109772.

References

[1] H. Cui, Y. Guo, W. Ma, et al., ChemSusChem 13 (2020) 1155–1171.
[2] C.C. Liu, X.J. Yan, F. Hu, et al., Adv. Mater. 30 (2018) 1705713.
[3] M. Acerce, D. Voiry, M. Chhowalla, Nat. Nanotechnol. 10 (2015) 313–318.
[4] C. Liu, Y. Bai, Y. Zhao, et al., Energy Storage Mater. 33 (2020) 470–502.
[5] Z.Y. Wang, Q.S. Tu, S.X. Zheng, et al., Nano Lett. 17 (2017) 7289–7298.
[6] F. Fan, R. Wang, W. Wu, et al., Chem. Soc. Rev. 50 (2021) 10983–11031.
[7] F.M. Ahmed, E.E. Ateia, A.S. Shafaay, et al., J. Energy Storage 82 (2024) 110360.
[8] G. Xu, X. Wang, Y. Sun, et al., Nano Res. 8 (2015) 2946–2953.
[9] Y. Wang, J. He, H. Pan, et al., Rare Met. 43 (2024) 1062–1071.
[10] L. Oakes, R. Carter, T. Hanken, et al., Nat. Commun. 7 (2016) 11796.
[11] X. Huang, J. Huang, P. Wu, et al., Adv. Sci. 8 (2021) 2101664.
[12] V. Augustyn, Y. Gogotsi, Joule 1 (2017) 443–452.
[13] Y. Shi, X. Zhao, Q. Liu, et al., Green Energy Environ. 9 (2024) 473–480.
[14] H.L. Tao, C. Lian, H.L. Liu, Green Energy Environ. 5 (2020) 303–321.
[15] S. Zhu, X. Zhao, Y. Shi, et al., Angew. Chem. Int. Ed. 62 (2023) e2023090.
[16] Y.Z. Zhang, J.K. El-Demellawi, Q. Jiang, et al., Chem. Soc. Rev. 49 (2020) 7229–7251.
[17] B. Lu, H. Cheng, L. Qu, ACS Nano 18 (2024) 2730–2749.
[18] A. Sikdar, P. Dutta, S.K. Deb, et al., Electrochim. Acta 391 (2021) 138959.
[19] X.W. Yang, L. Qiu, C. Cheng, et al., Angew. Chem. Int. Ed. 50 (2011) 7325–7328.

[20] Y. Cao, Z.Y. Xiong, F. Xia, et al., Adv. Funct. Mater. 32 (2022) 2201535.
[21] J.J. Wei, G. Wang, Y.J. Zhang, et al., Chin. Chem. Lett. 32 (2021) 1191–1196.
[22] J.J. Li, C.C. Liu, J.J. Wei, et al., Chin. Chem. Lett. 32 (2021) 880–884.
[23] H.H. Huang, Y. Cui, C.C. Dun, et al., Nano Energy 26 (2016) 172–179.
[24] Z.Y. Lin, Y. Liu, U. Halim, et al., Nature 562 (2018) 254–258.
[25] Y. Li, K.N. Duerloo, K. Wauson, et al., Nat. Commun. 7 (2016) 10671.
[26] C. Liu, X. Zhao, S. Wang, et al., ACS Appl. Energy Mater. 2 (2019) 4458–4463.
[27] D. Li, M.B. Müller, S. Gilje, et al., Nat. Nanotechnol. 3 (2008) 101–105.
[28] H. Yotsumoto, R. Yoon, J. Colloid Interface Sci. 157 (1993) 434–441.
[29] N.F. Zheng, X.H. Bu, P.Y. Feng, Nature 426 (2003) 428–432.
[30] K. Kang, S. Watanabe, K. Broch, et al., Nat. Mater. 15 (2016) 896–902.
[31] C.M. Palumbiny, F. Liu, T.P. Russell, et al., Adv. Mater. 27 (2015) 3391–3397.
[32] M.G. Viloria, G. Weick, D. Weinmann, R.A. Jalaber, Phys. Rev. B 88 (2013) 245428.
[33] X. Yang, C. Cheng, Y. Wang, et al., Science 341 (2013) 534–537.
[34] V. Augustyn, P. Simon, B. Dunn, Energy Environ. Sci. 7 (2014) 1597–1614.
[35] Y.F. Wang, X.W. Yang, A.G. Pandolfo, et al., Adv. Energy Mater. 6 (2016) 1600185.